JGR Solid Earth

RESEARCH ARTICLE
10.1029/2018JB017097

Water Migration in the Subduction Mantle Wedge: A Two-Phase Flow Approach

Hongliang Wang[1,2], **Ritske S. Huismans**[1], **and Stéphane Rondenay**[1]

[1]Department of Earth Science, University of Bergen, Bergen, Norway, [2]Now at Institute of Energy Technology, Oslo, Norway

Key Points:
- Water migration in the subduction zone is modeled by coupling two-phase flow theory and a dynamical subduction model
- Water release depth controls the distribution of water flux in the two main water pathways (trenchward and arcward) found in our models
- Our model results provide a geodynamical explanation for seismic observations in natural subduction environments

Supporting Information:
- Supporting Information S1
- Movie S1
- Movie S2
- Movie S3
- Movie S4
- Movie S5
- Movie S6
- Movie S7
- Movie S8
- Movie S9

Correspondence to:
H. Wang,
hongliangw@ife.no

Citation:
Wang, H., Huismans, R. S., & Rondenay, S. (2019). Water migration in the subduction mantle wedge: A two-phase flow approach. *Journal of Geophysical Research: Solid Earth*, *124*, 9208–9225. https://doi.org/10.1029/2018JB017097

Received 4 DEC 2018
Accepted 8 JUL 2019
Accepted article online 12 JUL 2019
Published online 14 AUG 2019

Abstract Subduction zones are the main entry points of water into Earth's mantle and play an important role in the global water cycle. The progressive release of water by metamorphic dehydration induces important physical-chemical processes, including subduction zone earthquakes. Yet, how water migrates in subduction zones is not well understood. We investigate this problem by explicitly modeling two-phase flow processes, in which fluids migrate through a compacting and decompacting solid matrix. Our results show that water migration is strongly affected by subduction dynamics, which exhibits three characteristic stages in our models: (1) an early stage of subduction initiation; (2) an intermediate stage of gravity-driven steepening of the slab; and (3) a late stage of quasi steady state subduction. Two main water pathways are found in the models: trenchward and arcward. They form in the first two stages and become steady in the third stage. Depending on the depth of water release from the subducting slab, water migration focuses in different pathways: a shallow release depth (e.g., 40 km) leads the water mainly through the trenchward pathway, a deep release depth (e.g., 120 km) promotes an arcward pathway and a long horizontal migration distance (~300 km) from the trench, and an intermediate release depth (e.g., 80 km) leads water to both pathways. We compare our models with seismic studies from southeast Japan (Saita et al., 2015, https://doi.org/10.1002/2015GL063084) and the west Hellenic subduction zone (Halpaap et al., 2018, https://doi.org/10.1002/2017JB015154) and provide geodynamical explanations for these seismic observations in natural subduction environments.

1. Introduction

Subduction zones are the major entry points for water recycling into the deep earth and play an important role in the global water cycle. Water released by the subducting slab has several consequences that affect the subduction system for a wide range of the timescale of million years (i.e., long-term subduction dynamics) to seconds (i.e., subduction seismicity): rheological weakening of the mantle (Hirth & Kohlstedt, 2003; Karato, 2010), serpentinization and other phase changes (Guillot et al., 2000; Poli & Schmidt, 2002), hydrous melting and arc magmatism (Davies et al., 1992), and high fluid pressure and embrittlement of deep mantle rocks (Hacker et al., 2003). Investigating the factors controlling water migration and distribution is therefore of paramount importance for understanding subduction dynamics.

Petrological and geophysical studies provide observations about the metamorphic dehydration and fluid migration in subduction zones. Water enters the subduction zone in mineral-bound form via hydrous phases (e.g., talc, amphibole, chlorite, and antigorite) within the oceanic lithosphere. As *P-T* conditions change during subduction, water is released from these minerals and occupies the pore space in the mantle due to dehydration reactions. Petrological experiments show that water is released over a large depth range in subduction zones: from ~30 km (1 GPa) to ~150 km (5 GPa; Fumagalli, 2004; Poli & Schmidt, 2002; e.g., Figure 1a). For natural subduction systems, the production of free water by dehydration is critically dependent on the thermal structure, the petrology of the subducting plate, and the distribution of hydrated minerals (Rondenay et al., 2008). Fluid distribution in the subduction mantle wedge can be estimated through geophysical inversion (Koulakov et al., 2016; McGary et al., 2014; Saita et al., 2015; Schurr et al., 2003; Soyer & Unsworth, 2006), which suggests the existence of fluid conductors or pathways. Based on seismic attenuation in southeast Japan (Figure 1b), Saita et al. (2015) inferred two high-fluid-content zones separated by a low-fluid-content zone above the subducting slab. Similar structures are also found in the Sunda/Sumatra subduction zone underneath the Toba volcano (Koulakov et al., 2016) and in the central Andean subduction zone (Schurr et al., 2003). These geophysical images clearly indicate a diversion of

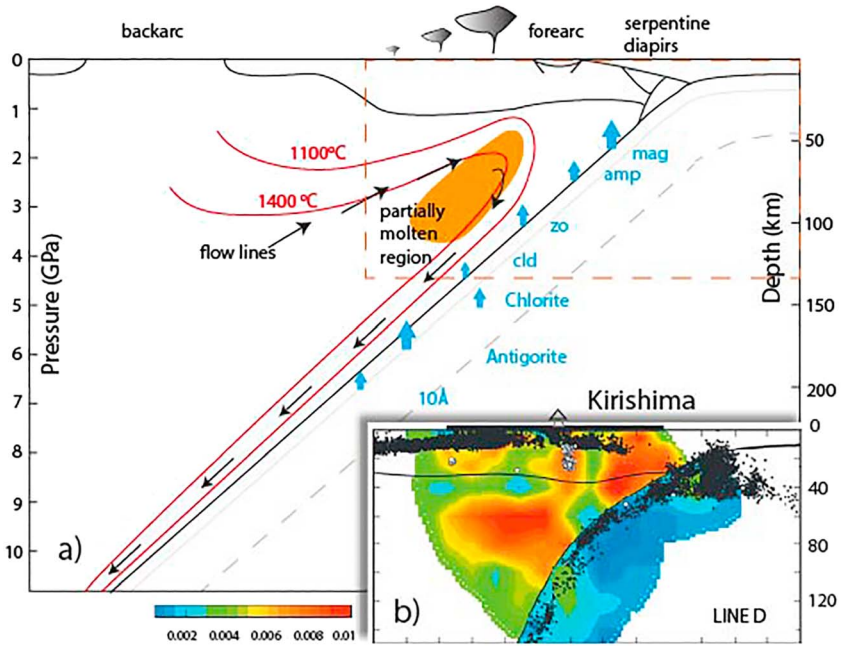

Figure 1. (a) Fluid-related processes in subduction zones from petrological studies (modified after Poli & Schmidt, 2002) and (b) seismic attenuation across a profile in southeast Japan (Saita et al., 2015). Water release at different depths from different hydrous minerals in the subduction zone are indicated with blue text and arrows.

fluid flow from vertically upward direction in these subduction zones. Some studies even suggest that fluid can migrate downward after its release from the slab (e.g., Faccenda et al., 2009; Hacker et al., 2003; van Keken et al., 2011). Despite these observations, the mechanisms that control fluid flow within the solid mantle are still unclear.

Geodynamic studies have adopted simplified approaches to model fluid migration, including a constant vertical percolation velocity (Arcay et al., 2006; Cagnioncle et al., 2007; Gerya & Meilick, 2010) and fluid flow driven by dynamic pressure (Li et al., 2015; Wada & Behn, 2015) or tectonic overpressure (non-lithostatic pressure) (Angiboust et al., 2012). These approaches are based on the dynamics of solid deformation and do not consider the migration of fluid through the (de)compaction of the solid rock, which is an important process of fluid transport in the solid earth (Audet & Fowler, 1992; Connolly & Podladchikov, 1998). Two-phase flow theory with compaction of the solid matrix was developed for earth materials over the past decades (Bercovici et al., 2001; Drew, 1983; McKenzie, 1984). It has been applied to sedimentary basin processes (e.g., Audet & Fowler, 1992; Morency et al., 2007) and magma dynamics (e.g., Katz et al., 2006; Keller et al., 2013). Recently, Wilson et al. (2014) investigated fluid migration in the kinematic subduction models by using two-phase flow, showing conditions that may lead to focused fluid flow. Zheng et al. (2016) studied the deformation patterns of the subduction interface and the effects of fluid flow by using two-phase flow modeling. These studies show that two-phase flow models provide a promising approach to study the migration of fluids and its potential effect on subduction dynamics. The understanding of solid-fluid interactions requires a self-consistent two-phase flow modeling approach.

In this study, we use a two-phase flow approach that couples fluid flow and solid deformation (Morency et al., 2007) in a dynamic subduction model (Currie et al., 2008) in order to investigate how water migrates and distributes in subduction zones with different control parameters. Our dynamical subduction model evolves with time as the velocity field is solved at every time step. The effects of water release depth, bulk viscosity, and permeability of the mantle are explored. We find that water distribution as inferred from the natural observations (Saita et al., 2015; Schurr et al., 2003) is reproduced by our models and provides a geodynamical explanation of water migration and distribution in subduction zones.

Table 1
Symbols and Parameter Values

Variable name	Symbol	Unit	Value
Porosity	ϕ	—	
Background porosity	ϕ_0	—	2×10^{-4}
Solid density	ρ_s	kg/m^3	
Fluid density	ρ_f	kg/m^3	10^3
Average density	$\rho = (1-\phi)\rho_s + \phi\rho_f$	kg/m^3	
Gravitational acceleration	g	m/s^2	9.81
Skeleton velocity	$\boldsymbol{V_s}$	m/s	
Fluid velocity	$\boldsymbol{V_f}$	m/s	
Darcy velocity	$\boldsymbol{q_D} = \phi(\boldsymbol{V_f} - \boldsymbol{V_s})$	m/s	
Fluid shear viscosity	μ_f	Pa s	2.6×10^{-4}
Reference permeability	k_0	m^2	
Hydraulic conductivity	$K = k\rho_f g/\mu_f$	m/s	
Bulk viscosity factor	η_b	Pa s	
Bulk viscosity	$\xi(\phi) = \eta_b/\phi$	Pa s	
Solid shear viscosity	η_s	Pa s	
Deviatoric stress tensor	$\boldsymbol{\tau_s}$	Pa	
Total pressure	$-tr(\boldsymbol{\sigma})/3$	Pa	
Fluid pressure	P_f	Pa	
Hydostatic fluid pressure	$P_h = \rho_f gh$	Pa	
Compaction pressure	$P_c = P - P_f$	Pa	
Lithostatic pressure	P_L	Pa	
Excess fluid pressure	$P_{\mathrm{ex}} = P_f - \rho_f gh$	Pa	
Temperature	T	°C	
Heat conductivity	k_t	W/m/K	2.25, 52
Heat capacity	C_p	J/kg/K	750, 1,250
Thermal diffusivity	$\kappa = k_t/\rho C_p$	m^2/s	

2. Model Descriptions

2.1. Governing Equation

The geodynamical two-phase flow model describes the deformation of the composite medium (solid + fluid), in which the incompressible fluid migrates through compaction and decompaction of the pore space (Bercovici et al., 2001; McKenzie, 1984). Morency et al. (2007) presented a fully coupled poroplastic model to study pore fluid flow in sedimentary basins. Here we use this modeling approach and incorporate it with a dynamic subduction model to study fluid migration in subduction zones. The governing equations of mass conservation, momentum conservation, and Darcy flow are (Keller et al., 2013; Morency et al., 2007)

$$\nabla\cdot\boldsymbol{V_s} = -\frac{P_c}{\xi} = -\frac{P-P_f}{\xi} \tag{1}$$

$$\nabla\cdot(1-\phi)\boldsymbol{\tau_s} - \nabla P + \rho g = 0 \tag{2}$$

$$\nabla\cdot\left(\frac{k}{\mu_f}\left(\nabla P_f - \rho_f g\right)\right) = -\frac{P-P_f}{\xi} \tag{3}$$

where $\boldsymbol{V_s}$ is the solid velocity, P_f is fluid pressure, ξ is bulk viscosity, ϕ is porosity, $\boldsymbol{\tau_s}$ is deviatoric stress tensor, P is dynamic pressure, ρ is average density, ρ_f is fluid density, g is gravity acceleration, k is permeability, and μ_f is fluid viscosity. All the parameters are listed and described in Table 1. The deviatoric stress tensor for the solid is defined as

$$\boldsymbol{\tau_s} = \eta_s\left(\nabla\boldsymbol{V_s} + \nabla^t\boldsymbol{V_s} - \frac{2}{3}\nabla\cdot\boldsymbol{V_s}\right) \tag{4}$$

The permeability k depends on many factors such as porosity, geometry, and interconnection of the pore space, grain size, and deformation of the solid (Kawano et al., 2011; Wark et al., 2003; Wark & Watson, 1998). Here, we use a cubic porosity-permeability relationship (Keller et al., 2013; Morency et al., 2007):

$$k = k_0\frac{\phi^3}{\phi_0{}^3} \tag{5}$$

Following Keller et al. (2013), we define the compaction pressure as

$$P_c = P - P_f \tag{6}$$

The excess fluid pressure is defined as (Morency et al., 2007)

$$P_{\mathrm{ex}} = P_f - \rho_f gh \tag{7}$$

The fluid pressure P_f can be eliminated by using equation (7), and thus we can solve equations (1)–(3) for $\boldsymbol{V_s}$, P, and P_{ex}. The average fluid velocity can be calculated based on $\boldsymbol{V_s}$ and P_{ex} (Morency et al., 2007):

$$\phi\boldsymbol{V_f} = \boldsymbol{q}_D + \phi\boldsymbol{V_s} = -K\nabla\left(\frac{P_{\mathrm{ex}}}{\rho_f g}\right) + \phi\boldsymbol{V_s} = -\frac{k}{\mu_f}\nabla(P_{\mathrm{ex}}) + \phi\boldsymbol{V_s} \tag{8}$$

The porosity (ϕ) evolves as a consequence of viscous compaction (Birchwood & Turcotte, 1994; Fowler & Yang, 1999; Morency et al., 2007):

$$\frac{1}{1-\phi}\frac{D\phi}{Dt} = -\frac{P-P_f}{\xi} \tag{9}$$

where ξ is the bulk viscosity (see below). Here, we ignore mechanical compaction.

Table 2
Material Parameters

Parameter	Upper/mid crust	Lower crust	Oceanic crust	Mantle	Weak seed
Plastic rheology					
C_0 (MPa)	2	0	0	0	2
φ_{eff} [a]	15° to 2°	15° to 2°	15° to 2°	15° to 2°	5°
Viscous rheology					
f	5	1	1	1 or 10 [b]	1
A (Pa^{-n} s^{-1})	8.57×10^{-28}	2.89639×10^{-28}	2.89639×10^{-28}	1.7578×10^{-28}	8.574×10^{-28}
n	4	4.7	4.7	3	4
Q (kJ/mol)	223	485	485	430	223
V (cm^3/mol)	0	0	0	10	0
Density parameters					
ρ_0 (kg/m^3)	2,800	2,950 (3,100)[c]	2,900 (3,300)[c]	3,250	3,250
T_0 (°C)	200	500 (500)[c]	0 (500)[c]	1,344	1,344
α (K^{-1})	3.0×10^{-5}	3.0×10^{-5}	3.0×10^{-5}	3.0×10^{-5}	3.0×10^{-5}
Thermal parameters					
k_t (W/m/K)	2.25	2.25	2.25	2.25 (52)[d]	2.25
C_p (J/kg/K)	750	750	750	1,250	1,250

[a]The two friction angles are used when the accumulated strain is less than 0.5 and larger than 1.5, respectively. The effective friction angle is linearly interpolated between the two values as the strain accumulates from 0.5 to 1.5. [b]The rheological parameters of wet olivine (Karato and Wu, 1993) are used for the mantle. $f = 1$ is used for the sublithospheric mantle, while $f = 10$ is used for the lithosphere, including both continental and oceanic mantle lithosphere. [c]Values in the brackets are used when the phase changes at the eclogite stability field (Hacker, 2013). This includes the effects of the phase change (ecologization) of the oceanic crust and lower continental crust. [d]High value of thermal conductivity (52) is use to calculate the initial thermal structure in order to mimic a convecting mantle.

The energy equation is solved to update the thermal field during the tectonic deformation in the subduction system. As the porosity is very small ($\ll 0.1$) in our model, we ignore the thermal effect of fluid migration. The energy equation can be written as

$$\frac{\partial T}{\partial t} + \boldsymbol{V}_s \cdot \nabla T = \nabla(\kappa \nabla T) + V_z\, \kappa g T\, \rho. \tag{10}$$

where κ is the thermal diffusivity and V_z is the vertical velocity. We use an arbitrary Lagrangian-Eulerian finite element technique (Fullsack, 1995; Morency et al., 2007) to solve the above equations.

2.1.1. Rheology

The deformation in a two-phase flow system comprises shear deformation and volumetric deformation. For the shear deformation of the solid, a viscoplastic rheology is used (Currie et al., 2008; Huismans & Beaumont, 2003). The flow is viscous when the deviatoric stress is below the frictional-plastic yielding stress, with an effective shear viscosity:

$$\eta_{\text{eff}} = f B I_2^{'(1-n)/n} \exp\left(\frac{E + PV}{nRT}\right) \tag{11}$$

where $I_2^{'}$ is the second invariant of the strain rate tensor $I_2^{'} = \left(\frac{1}{2}\dot{\varepsilon}_{ij}\dot{\varepsilon}_{ij}\right)^{1/2}$. f is a scaling factor (see Table 2). The pre-exponential factor $B = 2^{(1-n)/n}\, 3^{-(n+1)/2n}\, A^{-1/n}$ (see Table 2), which includes a conversion from the uniaxial laboratory experiments to the plane strain.

Frictional-plastic deformation is modeled with a Drucker-Prager yield criterion. Yielding occurs when the second invariant of the deviatoric stress $J_2^{'} = \left(\frac{1}{2}\tau_{ij}\tau_{ij}\right)^{1/2}$ calculated from the viscous flow (equation (4)) exceeds the yield stress:

$$\tau_{\text{yield}} = C_0 \cos(\varphi_{\text{eff}}) + P \sin \varphi_{\text{eff}} \tag{12}$$

An effective plastic viscosity is then defined as

Table 3
Comparison of Parameters in All Discussed Models

Model	Water release depth: d_R (km)	Bulk viscosity factor: η_b	Reference permeability: k_0 (m^2)
R	80	3×10^{22}	10^{-22}
M1	40	3×10^{22}	10^{-22}
M2	120	3×10^{22}	10^{-22}
M3	80	10^{22}	10^{-22}
M4	80	10^{23}	10^{-22}
M5	80	3×10^{22}	10^{-23}
M6	80	3×10^{22}	10^{-21}

$$\eta_{\text{eff}}^{p} = \frac{\tau_{\text{yield}}}{2I_2'} \tag{13}$$

Where C_0 is the cohesion, φ_{eff} is the effective internal friction angle, and P is the dynamic pressure. The Drucker-Prager failure criterion is equivalent to a Coulomb yield criterion for incompressible flow in 2-D plane strain with suitable adjustment of the constants (Huismans & Beaumont, 2003). We do not explicitly consider the effects of the fluid pressure on frictional-plastic yield in this study. In order to localize the deformation at the subduction interface, our model uses a strain weakening mechanism in which the friction angle linearly decreases from 15° to 2° over an accumulated strain from 0.5 to 1.5.

For the volumetric deformation, the bulk viscosity ξ is used to characterize the capacity of viscous compaction and decompaction of the solid matrix. The viscous compaction is related to pressure solution viscous creep, of which the constitutive law is poorly constrained. We adopt a viscous compaction law based on a constant bulk viscosity factor η_b, which ignores the effect of grain size and assumes no interconnecting pores (Connolly, 1997; Connolly & Podladchikov, 2000; McKenzie, 1984), and only consider the change of bulk viscosity caused by the change of porosity. By varying η_b in different models (Tables 2 and 3), we are able to study the effects of bulk viscosity.

$$\xi = \frac{\eta_b}{\phi} \tag{14}$$

2.2. Model Setup

The setup of our subduction model is similar to that of previous studies (e.g., Currie et al., 2008; Warren et al. 2008), except for the fact that every solid material is assigned a porosity (volume of the water) and can compact/decompact when the fluid migrates through the solid matrix. Figure 2 shows the material setup and boundary conditions for both the solid dynamics and two-phase flow, which will be described separately.

2.2.1. Subduction Setup

The initial geometry of the material setup and boundary conditions for the momentum and energy equations are shown in Figure 2. The model domain is 2,000 by 660 km. It is discretized with 400-by-160 finite elements and ~1 million Lagrangian particles. We refine the mesh vertically so that it has a resolution of 5 km (horizontal) by 1.8 km (vertical) in the top 180 km of the model domain. The continental lithosphere consists of a 24-km thick upper continental crust, 12-km thick lower crust, and 84-km thick mantle lithosphere, while the oceanic lithosphere is composed of 9-km thick oceanic crust and 81-km thick oceanic lithosphere. The properties of the materials used in the model are listed in Table 2. The top boundary is a free surface,

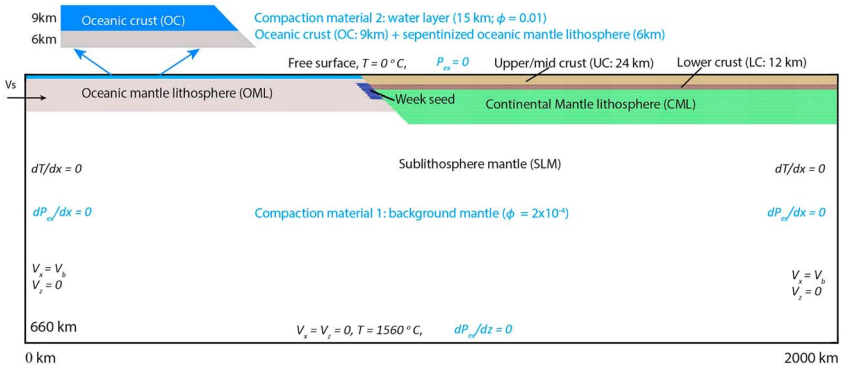

Figure 2. Initial material setup and boundary conditions for the solid subduction model (black text) and for the fluid flow (blue text). The layered oceanic and continental lithosphere are indicated with different colors, while sublithospheric mantle is white. Inset at top shows compaction material 2, which is the top 15 km of the oceanic lithosphere. All other areas, including the sublithospheric mantle, are compaction material 1.

where surface processes are not considered. The movement of the oceanic plate is kinematically imposed at the left boundary, and a weak seed allows the initiation of subduction (Figure 2). The side boundaries of the sublithospheric mantle are open with a small uniform outflow to maintain the total mass in the model. The temperature is fixed at the surface (0 °C) and bottom (1560 °C), while zero heat flux is applied at the side boundaries. The initial thermal structure is calculated as a result of the steady-state thermal field with these boundary conditions and material thermal parameters in Table 2.

2.2.2. Two-Phase Flow Setup

The initial and boundary conditions for two-phase flow are indicated in Figure 2. The Darcy flow is solved with the excess pressure $P_{ex} = P_f - \rho gh$. Zero pressure gradient is applied to the side boundaries and basal boundary, while fixed excess pressure (0) is applied on the surface. We use two compaction materials for all solid materials (e.g., Figure 2): (1) the background material with an initial porosity of $\phi_0 = 2 \times 10^{-4}$ and (2) a water-bearing layer in the subduction slab with an initial porosity of $\phi_0 = 0.01$, which includes 9-km oceanic crust and 6-km hydrated oceanic mantle lithosphere. As the water-bearing layer is subducting into the mantle, water is released from the slab and feeds into the surrounding mantle. The porosity of the whole system thus evolves when the water migrates through the mantle. To maintain a stable porosity at the bottom of the model, we fix the porosity of the elements in the lowest 20 km to be constant through time. This mimics a constant water reservoir at the bottom of the model. The parameters for the two-phase flow are given in Table 1.

Instead of considering complex processes of metamorphic dehydration, we use a simple depth- and material-dependent compaction property to release water in our model. A standard bulk viscosity factor η_b and reference permeability k_0 are used for compaction material 1, which represents the background mantle. Compaction material 2 has the same reference η_b and k_0 when it passes below a certain depth threshold, which we call the water release depth d_R, but above this depth η_b is 10^5 times higher and k_0 is 10^5 times lower than the respective reference values. Through the depth-dependent compaction property, compaction material 2 is able to maintain its high water content at shallow depth, which mimics water bound in hydrated minerals, and can release water beyond the water release depth, which mimics pressure- and temperature-dependent dehydration processes. We also increase the bulk viscosity factor η_b of the oceanic lithosphere by a factor of 100 in order to focus on the water migration in the mantle wedge. By using a different water release depth in the various models, we mimic the dehydration processes that may occur at different depths due to different dehydration reactions.

A range of values for η_b and k_0 (Table 3) are used in different models in order to study their effects on water migration. The ranges of these two parameters are chosen based on our current knowledge about fluid migration in subduction zones. The bulk viscosity is not well constrained by the experiments, but its porosity dependence (e.g., equation (14)) is generally assumed and widely used (Bercovici et al., 2001; Connolly et al., 2009; McKenzie, 1984; Miller et al., 2014; Morency et al., 2007). The permeability of the mantle is constrained by experimental data for a higher porosity than in our models. The reference permeability k_0 we use (10^{-23} to 10^{-21} m^2 for a porosity of 2×10^{-4}) is similar to Connolly (1997) and consistent with the extrapolation of the experimental studies (e.g., Connolly et al., 2009; McKenzie, 1984; Miller et al., 2014; Zhu et al., 1995). The compaction length scale in our reference model at background porosity of ϕ_0 is ~7.6 km, while the water pathways have higher background porosity and thus a larger compaction length. With a vertical resolution of 1.8 km per element, we can resolve the fluid migration in the water pathways quite well.

3. Results

A series of models with different parameters have been calculated in this study. In all cases, we begin by running the model for ~6 Myr, during which the subduction initiates but water migration and release are suppressed. We then restart the models with different water migration parameters as shown in Table 3 and run them for several tens of million years. In this section, we first present the reference model R, for which the water migration properties are set to the average values of all the models tested (see Table 3): $d_R = 80$ km, $\eta_b = 3 \times 10^{22}$ Pa s, $k_0 = 10^{-22}$ m^2. We describe the subduction dynamics with the material field of model R (Figure 3) and use this first set of results to show how water migrates during subduction (Figure 4). We then present and discuss Models M1–M5, which investigate the effects of water release depth, bulk viscosity, and permeability (Table 3) on water migration during subduction.

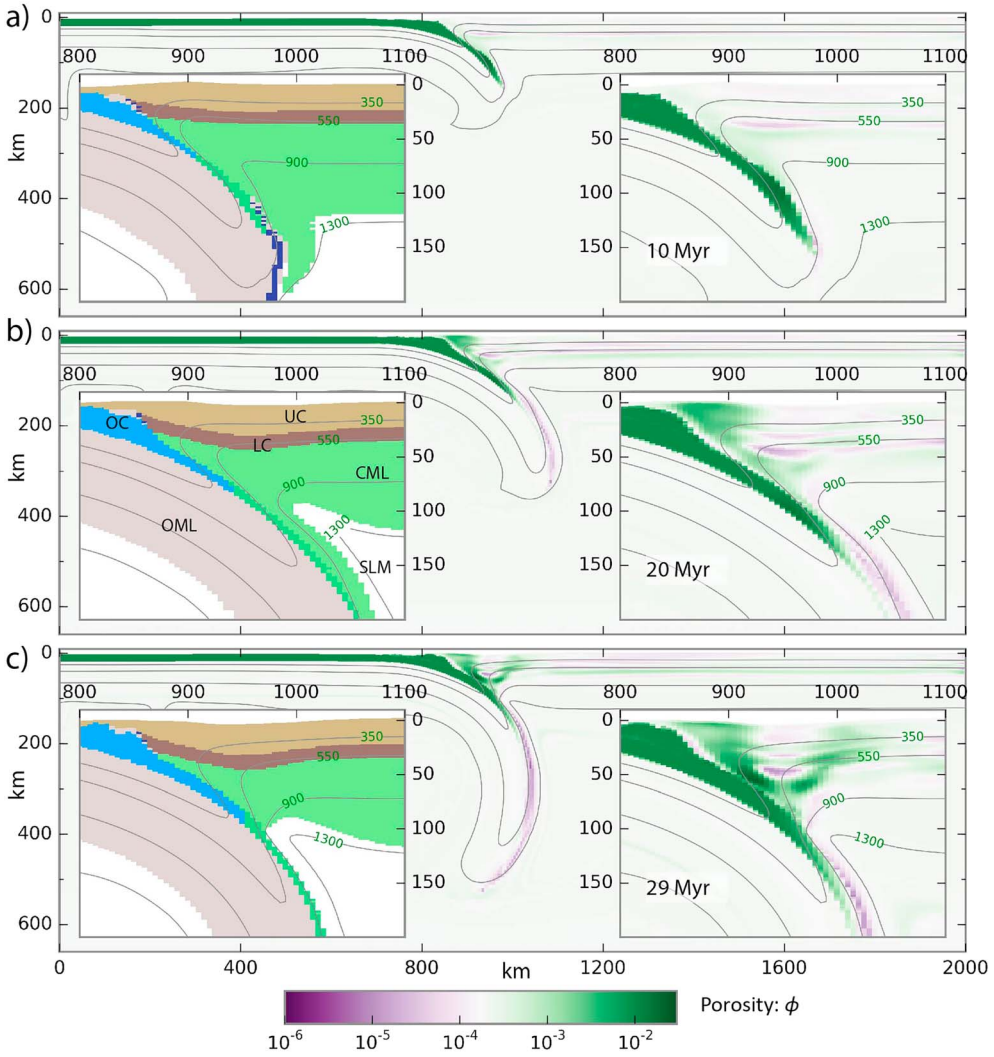

Figure 3. Porosity and material evolution for the reference model R at (a) 11 Myr, (b) 20 Myr, and (c) 29 Myr. The background plot shows porosity for the whole model domain, while the two insets show porosity (right) and material (left) fields, respectively. The 350, 550, 900, and 1350 °C isotherms are given with gray lines. During subduction, the water layer subducts into the mantle and water release starts at the depth of 80 km, where it feeds into the surrounding mantle.

3.1. Reference Model

The evolution of the reference model is characterized by three stages: (1) subduction initiation (0–10 Myr), (2) slab steepening (10–29 Myr), and (3) quasi steady state subduction (>29 Myr). During stage 1, subduction initiates by the imposed velocity of the oceanic slab and localized shear at the ocean-continent boundary facilitated by the inclined weak seed (Figure 2). During subduction initiation, the oceanic slab is bent underneath the overriding lithosphere and drags some continental lithosphere with it (Figure 3a). During stage 2, the dragged continental lithosphere peels away from the overriding lithosphere and the subducting slab steepens (Figures 3b and 3c). This is accompanied by a thickening of the oceanic crust in the shallow part of the subduction interface. Stage 3 from $t > 29$ Myr comprises stable subduction without significant change of the material field (Figure 3c). At this stage, the basaltic oceanic crust (blue) disappears when it is transformed into eclogite—that is, when it reaches the pressure-temperature condition corresponding to the stability field of eclogite.

The porosity evolution is strongly linked to the three stages of the subduction (Figure 3). During stage 1, the hydrated water-bearing layer subducts until it reaches 150-km depth. Compaction of the hydrated layer at depths larger than 80 km leads to initial transport of fluid along and above the subduction interface and a

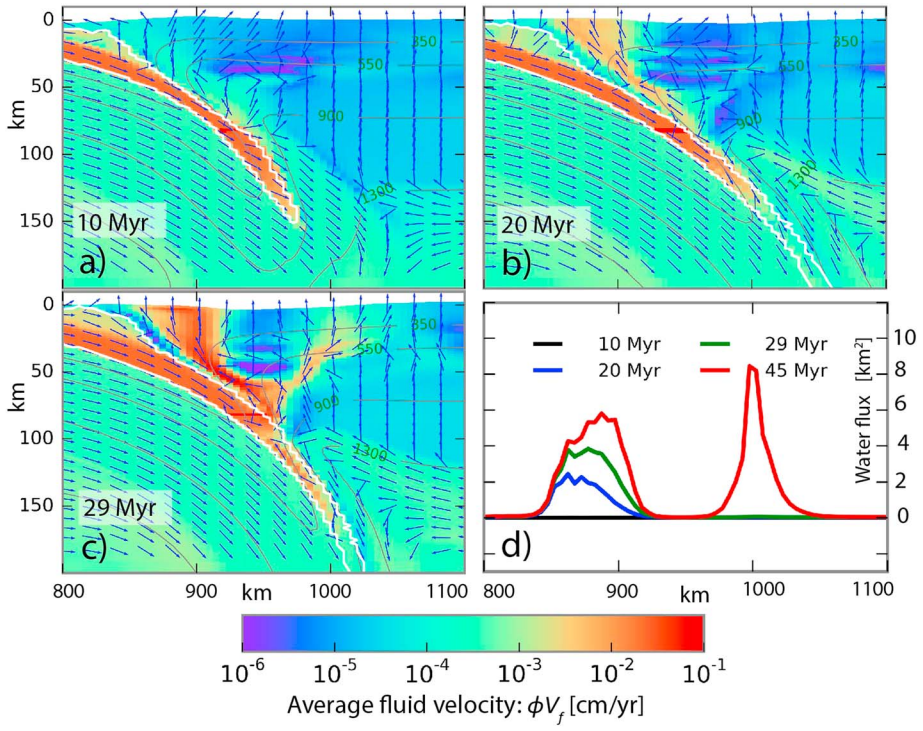

Figure 4. Evolution of average fluid velocity at (a) 11 Myr, (b) 20 Myr, (c) 29 Myr, and (d) water fluxes at the surface through time in the reference model R. The blue arrows show the direction of fluid velocity. Note two peaks in water fluxes which correspond to two main water pathways.

quasi-horizontal high-porosity zone in the overlying lithosphere at ~60-km depth. During stage 2, fluid release from the subducting hydrated material beyond the water release depth results in a well-established high-porosity zone in the trench area and within the mantle wedge (Figures 3b and 3c). At the end of stage 2, a second arcward fluid pathway is established, leading upward from the horizontal high-porosity zone within the mantle wedge (Figure 3c). The two fluid pathways are separated by a lower-porosity zone (hereafter referred to as the "low-porosity divide") in the downward bent part of the uppermost mantle lithosphere.

The average fluid velocity and cumulative water flux at the surface through time are calculated from the porosity field (equation (8); see also supporting information) and presented in Figure 4. The fluid velocity field (Figures 4a–4c) confirms the three-stage fluid flow evolution with formation of the trenchward pathway during stages 1 and 2 and the establishment of the arcward pathway at the end of stage 2. The maximum fluid velocity (ϕV_f) is ~0.1 cm/year (Figure 4), implying an absolute fluid velocity ($\boldsymbol{V}_f$) of ~0.1 m/year. The cumulative water flux at the surface (Figure 4d) shows that most fluid reaches the surface along the trench and the arcward pathways, separated by a domain with negligible flux above the low-porosity mantle wedge (e.g., Figure 3c). The second peak at ~1,000 km clearly demonstrates that water migrates ~250 km away from the trench through the trenchward pathway in this model.

3.2. Effects of Water Release Depth

Models M1 and M2 test the effects of varying water release depth from 40 km (M1) to 120 km (M2; Figure 5). With a water release depth of 40 km, model M1 forms only one water pathway in the trenchward direction. In contrast, model M2 forms two water pathways as in the reference model R, but it channels more water in the arcward pathway. The common feature of the three models is the low-porosity divide above the slab at ~50-km depth and ~950 km on the horizontal axis. The low-porosity divide thickens and shortens from 11 to 29 Myr (Figure 5), during which the overriding lithosphere bends and the slab steepens (Figure 3). Though they release water at different depths, models M1 and M2 produce fluid velocities that share common traits with model R: above the release depth, the fluid is advected with the subducting slab; below the release

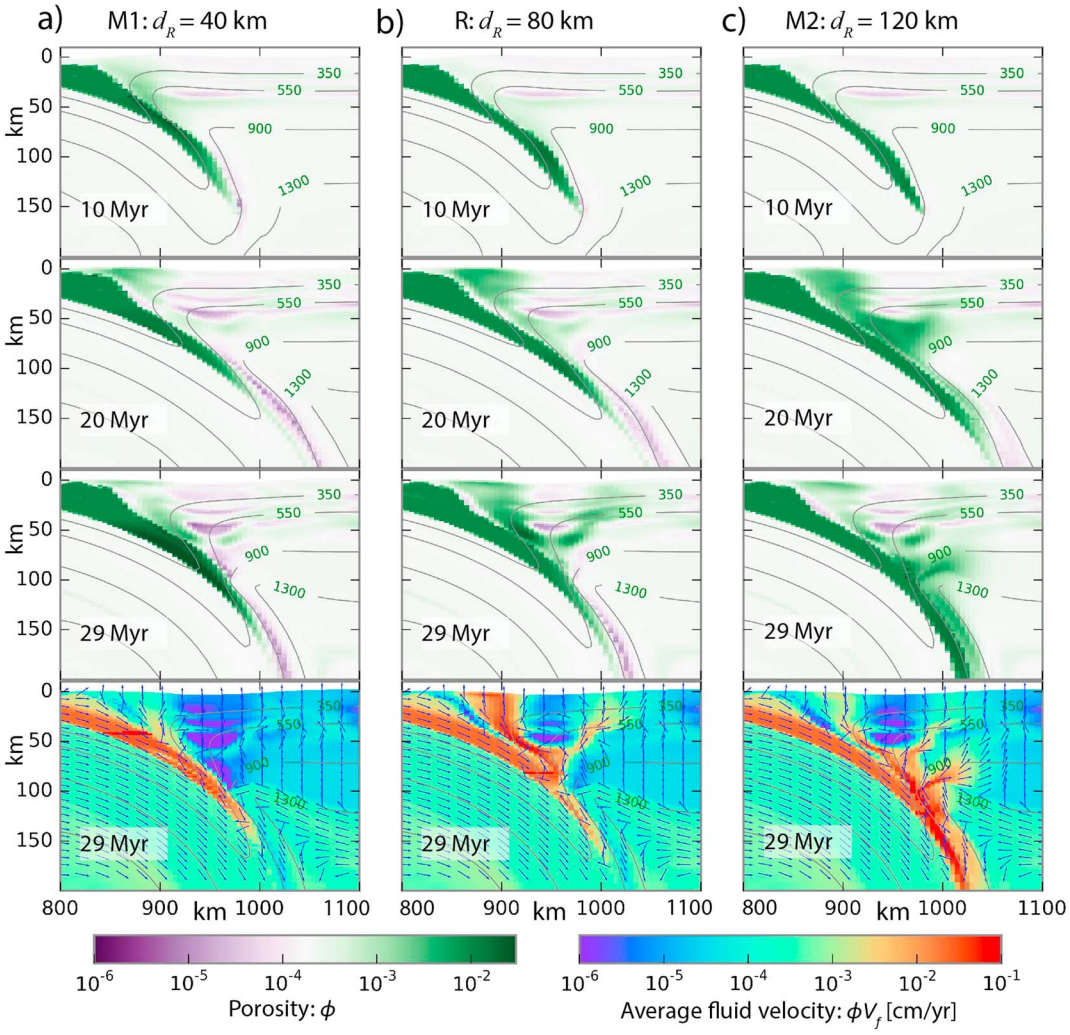

Figure 5. Porosity evolution (11, 19, and 29 Myr) and fluid velocity (29 Myr) for models with different water release depths: (a) M1: $d_R = 40$ km, (b) R: $d_R = 80$ km, (c) M2: $d_R = 120$ km. Porosity and fluid velocity show that shallow release depth promotes a trenchward pathway for fluid transport, while a deep release depth promotes an arcward pathway.

depth, the fluid flow deviates from the slab velocity and tends to migrate upward to the overlying lithosphere. In models M1 and R, the release depth is above the base of the lithosphere-asthenosphere boundary as defined by the 1300 °C isotherm Lithosphere-Asthenosphere Boundary (LAB). For this scenario, all the water released from the hydrated layer feeds into the overlying lithosphere (Figures 5a and 5b) and migrates mainly according to the Darcy velocity since the solid velocity is negligible in the overlying lithosphere in our models. In contrast, in model M2, with a water release depth of 120 km, water feeds into asthenosphere that has strong downward velocities. The downward solid velocity in the asthenosphere drags the water down until the porosity increases and the upward Darcy fluid velocity surpasses the effect of the solid velocity, leading the water upward into the corner of the mantle wedge and feeding it into the overlying lithosphere (Figure 5c). With the porosity, pressure and temperature fields, we estimate the melt fraction at 29 Myr for these three models and find higher degree of partial melting in model M2 with deep release depth (see supporting information).

3.3. Effects of the Bulk Viscosity

The sensitivity to bulk viscosity is investigated by models M3 and M4 (Figure 6), which have bulk viscosity factors 3 times higher and lower, respectively, than the reference model. The three models have the same water release depth. This means that the water feeds into the overlying lithosphere at the same point and forms the

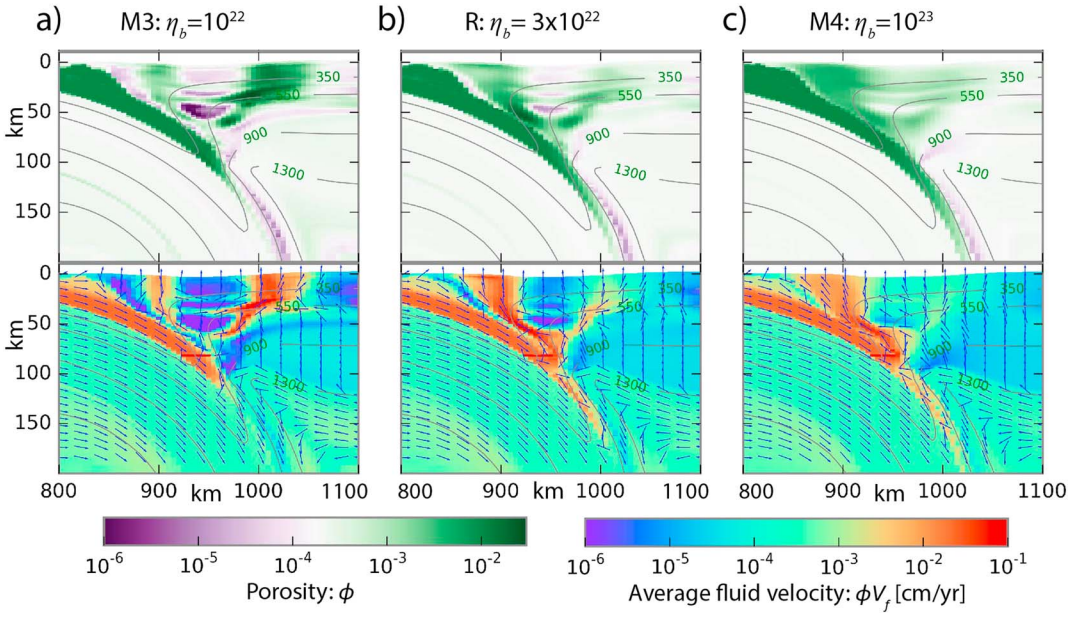

Figure 6. Comparison of three models with different bulk viscosity factors at 29 Myr: (a) M3: $\eta_b = 10^{22}$ Pa s, (b) R: $\eta_b = 3 \times 10^{22}$ Pa s, (c) M4: $\eta_b = 10^{23}$ Pa s. A low bulk viscosity factor leads to more focused porosity and fluid velocity field in model M3. A high bulk viscosity factor results in a smoother porosity and fluid velocity field in model M4.

two fluid pathways in all three models. The lower bulk viscosity model M3 ($\eta_b = 10^{22}$ Pa s, Figure 6a) shows a reduced porosity ($<10^{-4}$) at the base of the trench pathway and very low porosity ($<10^{-5}$) in low-porosity divide that separates the two pathways. In comparison, the higher bulk viscosity model M4 ($\eta_b = 10^{23}$ Pa s, Figure 6b) exhibits a much smoother porosity structure and a dominant trench fluid pathway. In the low-porosity divide, the porosity is not significantly reduced and stays at the background level (2×10^{-4}). The comparison of the three models suggests that lower bulk viscosity promotes more localized fluid flow.

3.4. Effects of the Permeability

Next, we test the sensitivity of our models to variations in the reference permeability k_0. To do so, we run two models, M5 and M6, in which the reference value of k_0 is increased and reduced, respectively, by a factor of 10 (see Figure 7). In model M5, which has a lower reference permeability $k_0 = 10^{-23}$m^2, water feeds into overlying lithosphere at the same feeding point as in the reference model R (i.e., 80-km depth), but its migration is impeded. The water accumulates and forms an area of higher porosity (>0.01) above the subduction interface (Figure 7a). Little water migrates up to the surface after 29 Myr of subduction. Conversely, the porosity level in the mantle wedge is much lower in model M6, which has a high reference permeability of $k_0 = 10^{-21}$m^2. Compared to model R, model M6 has a lower porosity level in both water pathways ($<10^{-3}$) and in the low-porosity divide ($<10^{-5}$), while model M5 shows the opposite. Thus, from a dynamical standpoint, a low reference permeability k_0 leads to high porosity levels (M5), whereas a high reference permeability k_0 results in lower porosity levels (M6) across the fluid pathways. However, despite their different porosity levels, we note that the three models exhibit a similar maximum fluid velocity of ~0.1 cm/year in their water pathways (cf., lower panels of Figures 7a–7c). This is due to the regulating effects of the porosity and reference permeability on the fluid velocity (equation (5)). The inverse relationship between k_0 and ϕ observed in models M5 and M6 therefore means that an increase in one of the two variables will be compensated by a decrease of the other.

3.5. Water Flux and the Average Porosity

We next compare the water flux at the surface and evolution of the average porosity of the three sets of models (Figure 8). The water release depth plays a major role on the partitioning/distribution of water flux in each pathway: A shallow release depth of 40 km leads water mainly to the trenchward pathway (model M1); an intermediate release depth of 80 km feeds water to both pathways (reference model R); a deep release depth of 120 km promotes the arcward pathway (model M2) (Figure 8a). The bulk viscosity affects

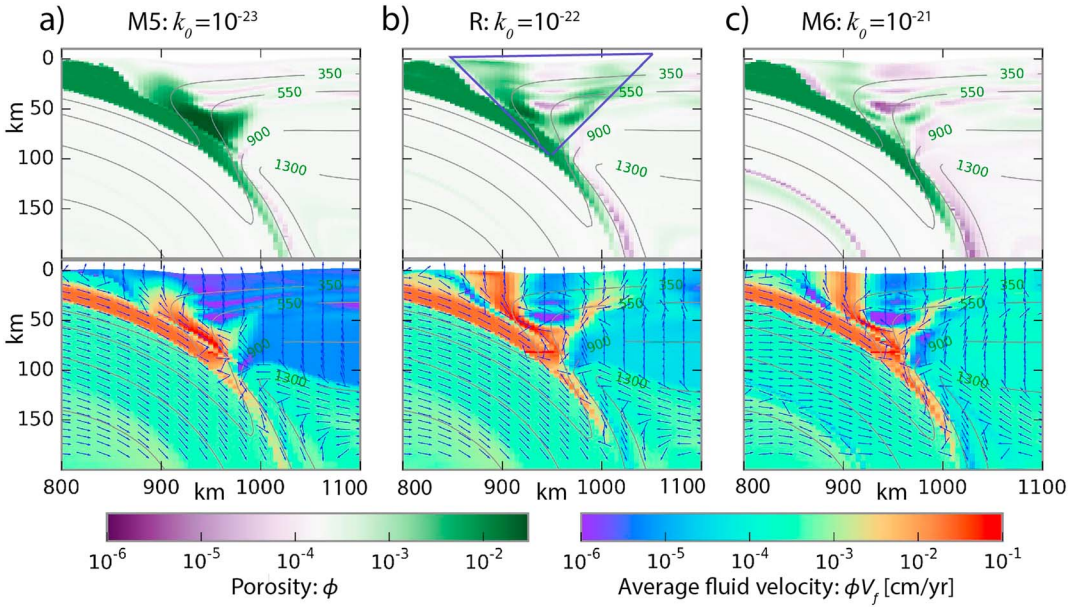

Figure 7. Comparison of three models with different reference permeabilities: (a) M5: $k_0 = 10^{-23}$ m^2, (b) R: $k_0 = 10^{-22}$ m^2, (c) M6: $k_0 = 10^{-21}$ m^2. A low permeability leads to high porosities in model M5, while a high permeability results in lower porosity levels in model M6. The maximum fluid velocity is similar among the three models. The triangle area within blue line boundaries shows the mantle wedge area used for calculation of average porosity in Figure 8.

the spatial distribution of the water flux (Figure 8b): a lower bulk viscosity factor localizes the water flux in the trenchward pathway (M3), while a higher bulk viscosity factor reduces the water flux in the arcward pathway significantly (M4). This result fits with the porosity image in Figure 6. Varying the reference permeability (Figure 8c) also has a significant effect on the water pathways. Model M6, with a high reference permeability k_0, has more water flux in the trenchward pathway as compared to model R, while it still has substantial water flux in the arcward pathway. Conversely, Model M5, characterized by a lower reference permeability, has almost zero water flux in the arcward pathway at 45 Myr (Figure 8c), with most water migrating through the trenchward pathway before 45 Myr and the formation of arcward pathway being delayed (see supporting information).

The evolution of average porosity with time for the mantle wedge and overlying plate yields periodic variation of water migration among models. Indeed, as shown in Figure 8 (right column), the water migration in the mantle wedge is not constant but rather goes up and down over time with periodicities ranging between ~6 and ~20 Myr. This is a manifestation of porosity waves in the solid rock, which are scaled by the compaction timescale (see supporting information). The observed periodicities reflect the combined periodicity of the porosity waves in two water pathways for each model. A comparison of models M3, R, and M4 (Figure 8b) shows that the period of the variation in average porosity increases with the bulk viscosity, consistent with the expected dependence of the compaction timescale on the square root of η_b/k_0 (see equation (S4) in supporting information). The average porosity is also affected by variation in permeability (e.g., Figure 8c) with low permeability k_0 resulting in a high porosity level and, conversely, high permeability leading to a low porosity level in the mantle wedge.

4. Discussion

4.1. Development of Multiple Water Pathways

Our models show that water migration during subduction is not homogenous but may be localized along some water pathways. The model results are consistent with previous work on the role of fluid flow during subduction that suggests that viscous compaction may lead to focused migration of fluids in the mantle wedge (i.e., Connolly & Podladchikov, 2015; McKenzie, 1984; Wilson et al., 2014). Specifically, our water migration models in the subduction zone are characterized by two water pathways with a low-porosity divide in between.

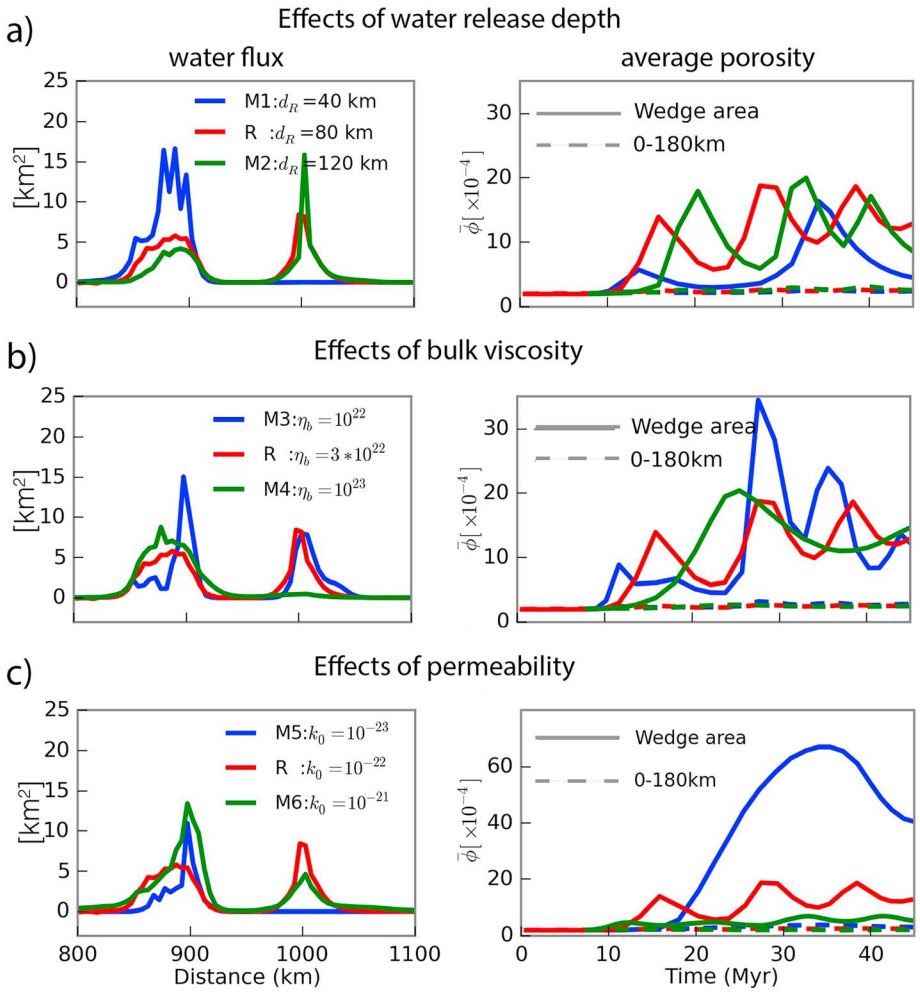

Figure 8. Comparison of surface water flux at 45 Myr (left column) and average porosity evolution through time (right column) for three groups of models. The effects of (a) water release depth, (b) bulk viscosity, and (c) permeability are investigated in these three groups of models. Average porosity is calculated in the mantle wedge area (as indicated in Figure 7b) and for 0- to 180-km depth for each model.

In contrast to the earlier work that modeled subduction with a kinematic approach (e.g., van Keken et al., 2002; Wilson et al., 2014), our model solves for the coupled solid deformation-viscous compaction-driven fluid migration problem, which allows for a more complete understanding of how these features develop. The dynamic and tectonic overpressure (Figure 9) provide insight into why the two separate fluid pathways with a low-porosity divide develop in our models. In the mantle wedge, the bending of the overlying lithosphere leads to a high dynamic and tectonic overpressure in the upper strongest part of the mantle lithosphere (Figures 9c and 9d), leading to a low lower-porosity zone. Fluid flow from beneath tends to avoid this high-pressure zone, which naturally results in two water pathways (Figure 9a). This suggests that variations in the dynamic and tectonic overpressure zones related to subduction dynamics can affect water migration. The tectonic overpressure predicted by the dynamic models ranges between −0.5 and 1 GPa, up to 50% of the lithostatic pressure, similar to the previous modeling studies of subduction dynamics (Gerya, 2015; Li et al., 2010; Schmalholz et al., 2014).

4.2. Water Flux Through Time and Space

The bulk viscosity and the permeability are the major parameters controlling compaction and efficiency of fluid migration. The compaction time scales with $\sqrt{\frac{\eta_b}{k_0}}$ (e.g., equation (S4) in supporting information), showing that the efficiency of fluid migration is proportional to $\sqrt{\eta_b}$ and inversely proportional to $\sqrt{k_0}$. Our model

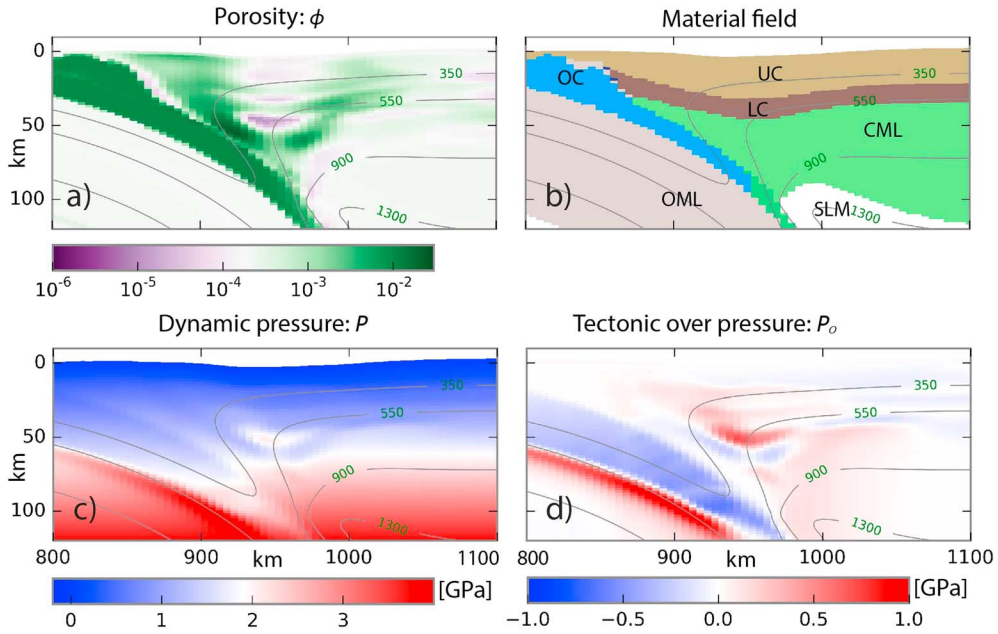

Figure 9. Reference model R represented in terms of (a) porosity, (b) material, (c) dynamic pressure, and (d) tectonic overpressure at 29 Myr. Note high dynamic pressure zone at the top of the strong overlying mantle lithosphere. Two water pathways develop on each side of this high-pressure area.

results show that a lower bulk viscosity factor η_b leads to a larger porosity contrast between the high- and low-porosity areas (Figures 6a–6c). This is due to the fact that lower bulk viscosity amplifies the (de) compaction of the skeleton matrix with more pore space opened and closed during fluid migration. Low permeability slows down water migration and results in water accumulation in the mantle wedge, explaining why a much higher porosity is produced in model M5 (Figure 7a). Higher permeability, in contrast, reduces the porosity as in model M6 (Figure 7c). While changes of the bulk viscosity and permeability during subduction in the real Earth are more complex than in our forward models, the results above allow us to understand the general effect of changes of these parameters on water migration.

The water release depth, on the other hand, is a first-order factor controlling water flux in the different pathways. Petrological studies have shown that water is released from the subducting slab over a large depth range (Figure 1a). The three water release depths (40, 80, and 120 km) in our models cover the release at shallow, intermediate, and large depths in the subduction zone, respectively. The effects of the water release depth based on our model results can be summarized as follows (see Figure 10). Water released at shallow depth promotes migration mainly through the trenchward pathway (Figure 10a). Intermediate depth water

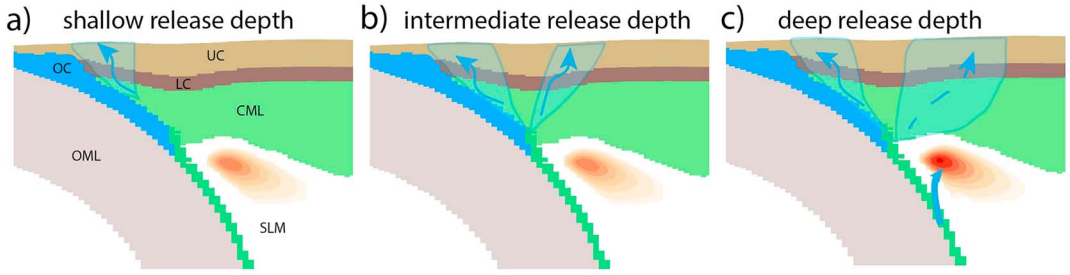

Figure 10. Diagram summarizing the effects of water release depth. Water release depth provides a first-order control on the formation of the trenchward and/or arcward fluid pathways. The orange color indicates the melt fraction estimated with the parameterization from Katz et al. (2006; see Figure S2 in the supporting information). Shallow and intermediate release depth promote a trenchward pathway and lead to hydration of the mantle wedge, while a deep release depth promotes an arcward fluid pathway and results in water in the asthenosphere that may cause hydrous melting and subduction volcanism. (a) Shallow release depth, (b) intermediate release depth, and (c) deep release depth.

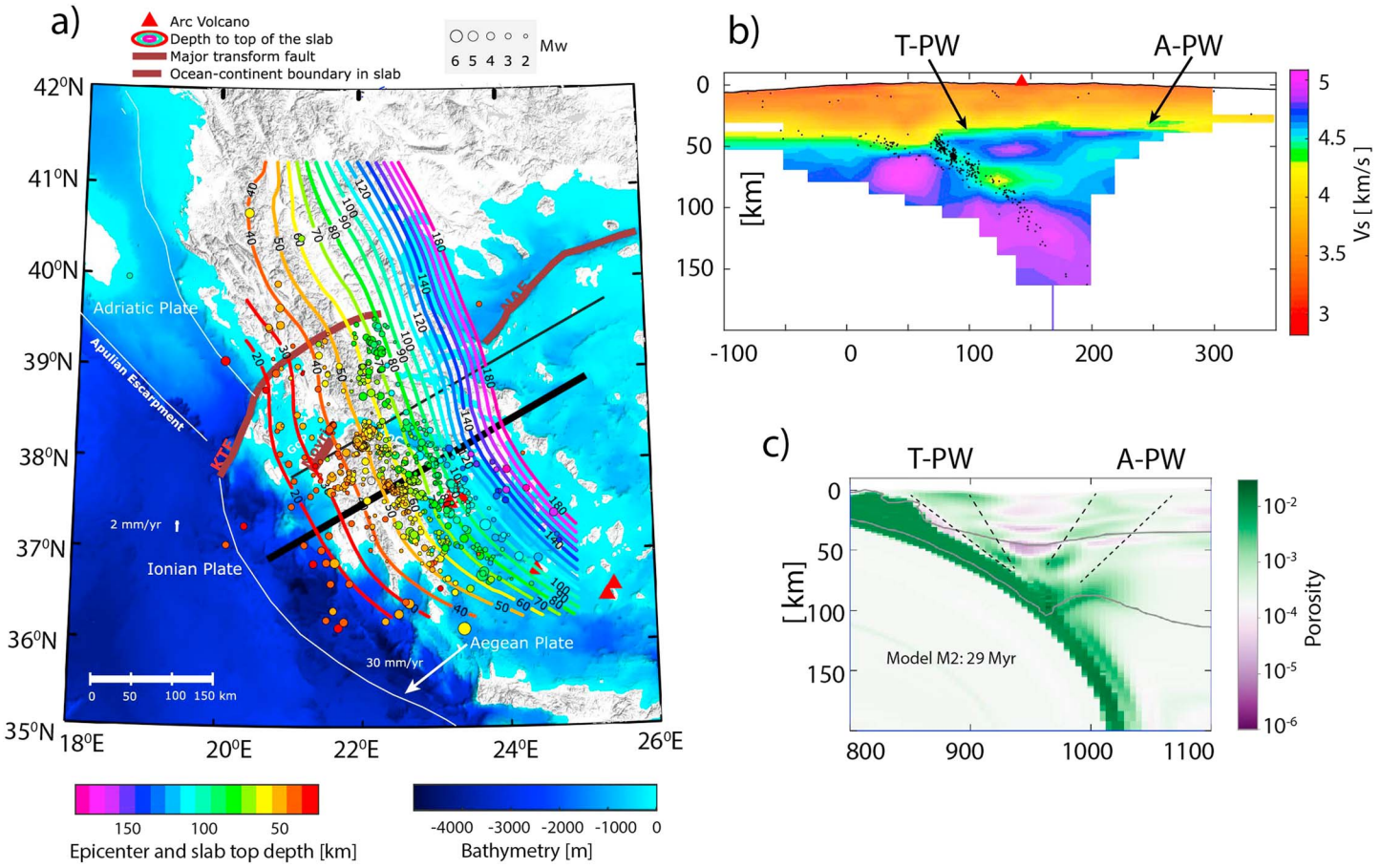

Figure 11. (a) Topography and bathymetry of Greece and the west Hellenic subduction zone. epicenters of earthquakes deeper than 35 km are plotted with circles, with size indicating earthquake magnitude and color indicating depth. (b) Shear wave velocity (V_S) image for cross-section indicated in (a). (c) Porosity for model M2 at 29 Myr. Comparison between (b) V_S and (c) porosity in the forward model shows strong similarities.

release promotes two water pathways with migration of fluids along the trench and into the arc, avoiding the high-pressure zone in the overlying lithosphere (Figure 10b). A deep release depth mainly feeds water into the asthenosphere at the subduction corner and fluid transport in an arcward pathway in the overlying lithosphere (Figure 10c). This deep fluid release would be expected to lead to hydrous melting (see Figure S2 in supporting information), not included in our modeling approach, which would absorb part or all of the available water (Figure 10c). As a consequence, while water release at shallow and intermediate depths is expected to primarily cause hydration of the mantle wedge, the water releases at large depths will contribute to subduction volcanism (e.g., Figure 10).

4.3. Implications for Natural Systems

Our models provide insight into factors controlling the migration and distribution of fluids in subduction zones and can help us better understand fluid distribution in the natural subduction systems as inferred from geophysical observations. The fluid distribution in southeast Japan subduction zone (e.g., Saita et al., 2015) has been explained as resulting from water released by dehydration at different *P-T* conditions and their corresponding depths. Our models may explain why the inferred water flow in this area appears to be diverted from the vertically upward direction and split into two main pathways—one toward the arc and another along the subduction interface (Figure 1b). As the dense oceanic plate subducts underneath the overriding plate, it induces strong horizontal and vertical gradients of the stress field in the subduction zone, which results in tectonic overpressure (e.g., Schmalholz et al., 2014). Our models demonstrate that high tectonic overpressure in the overlying lithosphere (Figure 9) drives the water away and thus diverts the water pathways from the vertically upward direction.

Observations from the western Hellenic subduction zone (Halpaap et al., 2018) suggest complex patterns of fluid migration into the mantle wedge and overriding lithosphere that are also consistent with our model results. The western Hellenic subduction zone (Figure 11a) is characterized by slow continental subduction in the north and faster oceanic subduction in the south (Pearce et al., 2012). The distribution of subduction-related earthquakes from north to south fits with the transition from continental to oceanic subduction. To the north, the continental slab releases small amounts of fluid and exhibits little to no intermediate-depth earthquake activity. Conversely, to the south, the oceanic slab releases large volumes of water and exhibits significant intermediate depth earthquake activity. When considered together, the seismic *S* wavespeed ($\boldsymbol{V}_s$) structure and earthquake hypocenters across the oceanic part of the system reveal that seismic activity forms a continuous band between ~40- and 140-km depths that parallels the slab (Figure 11b; Halpaap et al., 2018). The shallower portion of this seismicity band (<100-km depth) coincides with a low-$\boldsymbol{V}_s$ layer attributed to hydrated rock of the subducted basaltic crust. All these observations point to low velocities in this part of the system being associated with hydrated rocks or fluids, and to fluids as playing a key role in the nucleation of intraslab earthquakes. We find a compelling resemblance between this $\boldsymbol{V}_s$ structure and the porosity in model M2 (Figures 11b and 11c). The seismic image shows a narrow zone with high $\boldsymbol{V}_s$ above the slab at ~50-km depth (Figure 11b) that can be compared with the high-pressure/low-porosity zone in the model (cf., Figure 11c). The image also shows two well-defined, inclined low-$\boldsymbol{V}_s$ zones on either side of the high-$\boldsymbol{V}_s$ zone, which may be related to fluid migration paths as suggested by our model (Figure 11c). The arc is positioned above the northeastern edge of the high-$\boldsymbol{V}_s$ zone (Figure 11b), and it can be linked to water release in the hot asthenospheric portion of the mantle wedge (Figure 11c), where extensive hydrous melting is expected to occur. As the melts have a much larger shear viscosity (~10^5) than water, the compaction length of melt migration is much smaller, explaining why the fluid pathways of the melts may be less prone to being diverted by the high-pressure zone. The amplitude of the $\boldsymbol{V}_s$ anomalies shown in Figure 11 varies along strike (see Halpaap et al., 2018), reflecting varying water content between the northern and southern subducting slab and the potential effects of 3-D dynamics (see, e.g., Davies et al., 2016). Similar observations are made in the Andean subduction zone (Schurr et al., 2003).

4.4. Model Limitations and Further Work

Although we solve the fully coupled problem of porous compaction and associated viscous-plastic deformation of the solid matrix, the models presented here are purposely simple in their setup and consequently characterized by a number of limitations. For example, prograde metamorphic reaction in the slab may cause fluids to be released over a continuous depth range as opposed to being focused at singular locations as in our models. Moreover, variations in fluid content (e.g., water or melts) that may affect viscous flow in the mantle (Hirth & Kohlstedt, 1996; Karato, 2010), and cause phase changes such as serpentinization and eclogitization (Hacker et al., 2003; Poli & Schmidt, 2002) were not explicitly included. We furthermore assumed no chemical transport of solutes with the fluid phase, thus ignoring the effects of reactive transport—a process that is likely important for channelized reactive flows in nature (Arkwright et al., 2008; Plümper et al., 2017). The effect of fluid pressure on frictional yield, which may weaken for instance the subduction interface and lead to dehydration embrittlement (Jung et al., 2004; Podladchikov & Miller, 2013; Skarbek & Rempel, 2016), is also missing from our models. Lastly, future models could include grain-size-dependent and anisotropic permeability, which may play a role in the development of the fluid pathways in subduction zones (Cerpa et al., 2017; Kawano et al., 2011).

5. Conclusions

We use a numerical framework that couples porous compaction driven fluid flow with viscous-plastic deformation of the solid matrix to model the effects of water migration during subduction. Our results show that water migration is not homogeneous but localized along fluid pathways in the mantle wedge that are diverted from the vertical direction. Water migration occurs preferentially along the subduction interface from where it feeds into the mantle wedge. Two main water pathways are found: a trenchward and an arcward pathway. Our dynamical models demonstrate that it is the tectonic overpressure in the subduction system that diverts the water away from a purely vertical flow and forms two water pathways during subduction. The depth of water release from the subduction slab provides a first-order control on which pathway is used by water released from the subducting slab: A shallow release of water at 40 km results in

water migration mainly through the trenchward pathway; a deep release at 120 km results in most water transport through the arcward pathway with migration over a distance of 250 km from the trench; an intermediate release depth of 80 km leads water to both pathways. Our model results further show that the length scale and timescale of fluid migration depends on bulk viscosity and permeability. The two pathways shown in the forward models compare well with, and may explain, observations in natural subduction systems such as the west Hellenic subduction (Halpaap et al., 2018) and in southeast Japan (Saita et al., 2015).

Acknowledgments
We thank Felix Halpaap for providing the seismic images from his study and Nicolas Riel for the useful discussion about the two-phase flow modelling. We also thank Boris Kaus, Weronika Gorczyk, and the Editor for the insightful reviews, which helped to improve the manuscript. The data for this paper, including model data for the plots, plotting scripts, and the source code to calculate water content and porosity based on Perplex data can be accessed from Pangaea Data Archiving and Publication (https://doi.org/10.1594/PANGAEA.901802). The detailed description of numerical methods can be found in Morency et al. (2007) and its references, in order to fully reproduce the code and results. The study was supported by funding from the Research Council of Norway for the project "Subduction zone Water and Metamorphism: A Modelling and Imaging Study" (project 231354).

References

Angiboust, S., Wolf, S., Burov, E., Agard, P., & Yamato, P. (2012). Effect of fluid circulation on subduction interface tectonic processes: Insights from thermo-mechanical numerical modelling. *Earth and Planetary Science Letters*, *357-358*, 238–248. https://doi.org/10.1016/j.epsl.2012.09.012

Arcay, D., Doin, M.-P., Tric, E., Bousquet, R., & de Capitani, C. (2006). Overriding plate thinning in subduction zones: Localized convection induced by slab dehydration. *Geochemistry, Geophysics, Geosystems*, *7*, Q02007. https://doi.org/10.1029/2005GC001061

Arkwright, J. C., Rutter, E. H., Brodie, K. H., & Llana-Funez, S. (2008). Role of porosity and dehydration reaction on the deformation of hot-pressed serpentinite aggregates. *Journal of the Geological Society*, *165*(3), 639–649. https://doi.org/10.1144/0016-76492007-119

Audet, D. M., & Fowler, A. C. (1992). A mathematical model for compaction in sedimentary basins. *Geophysical Journal International*, *110*(3), 577–590. https://doi.org/10.1111/j.1365-246X.1992.tb02093.x

Bercovici, D., Ricard, Y., & Schubert, G. (2001). A two-phase model for compaction and damage: 1. General Theory. *Journal of Geophysical Research*, *106*(B5), 8887–8906. https://doi.org/10.1029/2000JB900430

Birchwood, R. A., & Turcotte, D. L. (1994). A unified approach to geopressuring, low-permeability zone formation, and secondary porosity generation in sedimentary basins. *Journal of Geophysical Research*, *99*(B10), 20,051–20,058. https://doi.org/10.1029/93JB02388

Cagnioncle, A.-M., Parmentier, E. M., & Elkins-Tanton, L. T. (2007). Effect of solid flow above a subducting slab on water distribution and melting at convergent plate boundaries. *Journal of Geophysical Research*, *112*, B09402. https://doi.org/10.1029/2007JB004934

Cerpa, N. G., Wada, I., & Wilson, C. R. (2017). Fluid migration in the mantle wedge: Influence of mineral grain size and mantle compaction. *Journal of Geophysical Research: Solid Earth*, 6247–6268. https://doi.org/10.1002/2017jb014046

Connolly, J., & Podladchikov, Y. (1998). Compaction-driven fluid flow in viscoelastic rock. *Geodinamica Acta*, *11*(2-3), 55–84. https://doi.org/10.1080/09853111.1998.11105311

Connolly, J. A. D. (1997). Devolatilization-generated fluid pressure and deformation-propagated fluid flow during prograde regional metamorphism. *Journal of Geophysical Research*, *102*(B8), 18,149–18,173. https://doi.org/10.1029/97JB00731

Connolly, J. A. D., & Podladchikov, Y. Y. (2000). Temperature-dependent viscoelastic compaction and compartmentalization in sedimentary basins. *Tectonophysics*, *324*(3), 137–168. https://doi.org/10.1016/S0040-1951(00)00084-6

Connolly, J. A. D., & Podladchikov, Y. Y. (2015). An analytical solution for solitary porosity waves: Dynamic permeability and fluidization of nonlinear viscous and viscoplastic rock. *Geofluids*, *15*(1-2), 269–292. https://doi.org/10.1111/gfl.12110

Connolly, J. A. D., Schmidt, M. W., Solferino, G., & Bagdassarov, N. (2009). Permeability of asthenospheric mantle and melt extraction rates at mid-ocean ridges. *Nature*, *462*(7270), 209–212. https://doi.org/10.1038/nature08517

Currie, C. A., Huismans, R. S., & Beaumont, C. (2008). Thinning of continental backarc lithosphere by flow-induced gravitational instability. *Earth and Planetary Science Letters*, *269*(3-4), 436–447. https://doi.org/10.1016/j.epsl.2008.02.037

Davies, D. R., Le Voci, G., Goes, S., Kramer, S. C., & Wilson, C. R. (2016). The mantle wedge's transient 3-D flow regime and thermal structure. *Geochemistry, Geophysics, Geosystems*, *17*, 78–100. https://doi.org/10.1002/2015GC006125

Davies, J. H., Huw Davies, J., & Stevenson, D. J. (1992). Physical model of source region of subduction zone volcanics. *Journal of Geophysical Research*, *97*(B2), 2037–2070. https://doi.org/10.1029/91JB02571

Drew, D. A. (1983). Mathematical modeling of two-phase flow. *Annual Review of Fluid Mechanics*, *15*(1), 261–291. https://doi.org/10.1146/annurev.fl.15.010183.001401

Faccenda, M., Gerya, T. V., & Burlini, L. (2009). Deep slab hydration induced by bendingrelated variations in tectonic pressure. *Nature Geoscience*. https://doi.org/10.1038/ngeo656

Fowler, A. C., & Yang, X. (1999). Pressure solution and viscous compaction in sedimentary basins. *Journal of Geophysical Research*, *104*(B6), 12,989–12,997. https://doi.org/10.1029/1998JB900029

Fullsack, P. (1995). An arbitrary Lagrangian-Eulerian formulation for creeping flows and its application in tectonic models. *Geophysical Journal International*, *120*(1), 1–23. https://doi.org/10.1111/j.1365-246X.1995.tb05908.x

Fumagalli, P. (2004). Experimentally determined phase relations in hydrous peridotites to 6.5 GPa and their consequences on the dynamics of subduction zones. *Journal of Petrology*, *46*(3), 555–578. https://doi.org/10.1093/petrology/egh088

Gerya, T. (2015). Tectonic overpressure and underpressure in lithospheric tectonics and metamorphism. *Journal of Metamorphic Geology*, *33*(8), 785–800. https://doi.org/10.1111/jmg.12144

Gerya, T. V., & Meilick, F. I. (2010). Geodynamic regimes of subduction under an active margin: Effects of rheological weakening by fluids and melts. *Journal of Metamorphic Geology*, *29*(1), 7–31.

Guillot, S., Hattori, K. H., & de Sigoyer, J. (2000). Mantle wedge serpentinization and exhumation of eclogites: Insights from eastern Ladakh, northwest Himalaya. *Geology*, *28*(3), 199–202. https://doi.org/10.1130/0091-7613(2000)28<199:MWSAEO>2.0.CO;2

Hacker, B. R. (2013). *Eclogite formation and the rheology, buoyancy, seismicity, and H_2O content of oceanic crust*, (pp. 337–346). Washington, DC: American Geophysical Union (AGU). https://doi.org/10.1029/GM096p0337

Hacker, B. R., Peacock, S. M., Abers, G. A., & Holloway, S. D. (2003). Subduction factory 2. Are intermediate-depth earthquakes in subducting slabs linked to metamorphic dehydration reactions? *Journal of Geophysical Research*, *108*(B1), 2030. https://doi.org/10.1029/2001JB001129

Halpaap, F., Rondenay, S., & Ottemöller, L. (2018). Seismicity, deformation and metamorphism in the western Hellenic subduction zone—New constraints from tomography. *Journal of Geophysical Research: Solid Earth*, *123*, 3000–3026. https://doi.org/10.1002/2017JB015154

Hirth, G., & Kohlstedt, D. (2003). *Rheology of the upper mantle and the mantle wedge: A view from the experimentalists*, *Geophysical Monograph Series*, (pp. 83–105). Washington, D. C: American Geophysical Union.

Hirth, G., & Kohlstedt, D. L. (1996). Water in the oceanic upper mantle: Implications for rheology, melt extraction and the evolution of the lithosphere. *Earth and Planetary Science Letters*, *144*(1-2), 93–108. https://doi.org/10.1016/0012-821X(96)00154-9

Huismans, R. S., & Beaumont, C. (2003). Symmetric and asymmetric lithospheric extension: Relative effects of frictionalplastic and viscous strain softening. *Journal of Geophysical Research*, *108*(B10), 2496. https://doi.org/10.1029/2002jb002026

Jung, H., Green, H. W. II, & Dobrzhinetskaya, L. F. (2004). Intermediate-depth earthquake faulting by dehydration embrittlement with negative volume change. *Nature*, *428*(6982), 545–549. https://doi.org/10.1038/nature02412

Karato, S., & Wu, P. (1993). Rheology of the upper mantle: A synthesis. *Science*, *260*(5109), 771–778. Retrieved from. http://www.ncbi.nlm.nih.gov/pubmed/17746109, https://doi.org/10.1126/science.260.5109.771

Karato, S.-I. (2010). Rheology of the deep upper mantle and its implications for the preservation of the continental roots: A review. *Tectonophysics*, *481*(1-4), 82–98. https://doi.org/10.1016/j.tecto.2009.04.011

Katz, R. F., Spiegelman, M., & Holtzman, B. (2006). The dynamics of melt and shear localization in partially molten aggregates. *Nature*, *442*(7103), 676–679. https://doi.org/10.1038/nature05039

Kawano, S., Katayama, I., & Okazaki, K. (2011). Permeability anisotropy of serpentinite and fluid pathways in a subduction zone. *Geology*, *39*(10), 939–942. https://doi.org/10.1130/G32173.1

Keller, T., May, D. A., & Kaus, B. J. P. (2013). Numerical modelling of magma dynamics coupled to tectonic deformation of lithosphere and crust. *Geophysical Journal International*, *195*(3), 1406–1442. https://doi.org/10.1093/gji/ggt306

Koulakov, I., Kasatkina, E., Shapiro, N. M., Jaupart, C., Vasilevsky, A., el Khrepy, S., et al. (2016). The feeder system of the Toba supervolcano from the slab to the shallow reservoir. *Nature Communications*, *7*(1), 12228. https://doi.org/10.1038/ncomms12228

Li, Z., Liu, M., & Gerya, T. (2015). Material transportation and fluid-melt activity in the subduction channel: Numerical modeling. *SCIENCE CHINA Earth Sciences*, *58*(8), 1251–1268. https://doi.org/10.1007/s11430-015-5123-5

Li, Z. H., Gerya, T. V., & Burg, J.-P. (2010). Influence of tectonic overpressure on *P-T* paths of HP-UHP rocks in continental collision zones: Thermomechanical modelling. *Journal of Metamorphic Geology*, *28*(3), 227–247. https://doi.org/10.1111/j.1525-1314.2009.00864.x

McGary, R. S., Evans, R. L., Wannamaker, P. E., Elsenbeck, J., & Rondenay, S. (2014). Pathway from subducting slab to surface for melt and fluids beneath Mount Rainier. *Nature*, *511*(7509), 338–340. https://doi.org/10.1038/nature13493

McKenzie, D. (1984). The generation and compaction of partially molten rock. *Journal of Petrology*, *25*(3), 713–765. https://doi.org/10.1093/petrology/25.3.713

Miller, K. J., Zhu, W.-L., Montési, L. G. J., & Gaetani, G. A. (2014). Experimental quantification of permeability of partially molten mantle rock. *Earth and Planetary Science Letters*, *388*, 273–282. https://doi.org/10.1016/j.epsl.2013.12.003

Morency, C., Huismans, R. S., Beaumont, C., & Fullsack, P. (2007). A numerical model for coupled fluid flow and matrix deformation with applications to disequilibrium compaction and delta stability. *Journal of Geophysical Research*, *112*, B10407. https://doi.org/10.1029/2006JB004701

Pearce, F. D., Rondenay, S., Sachpazi, M., Charalampakis, M., & Royden, L. H. (2012). Seismic investigation of the transition from continental to oceanic subduction along the western Hellenic subduction zone. *Journal of Geophysical Research*, *117*, B07306. https://doi.org/10.1029/2011JB009023

Plümper, O., John, T., Podladchikov, Y. Y., Vrijmoed, J. C., & Scambelluri, M. (2017). Fluid escape from subduction zones controlled by channel-forming reactive porosity. *Nature Geoscience*, *10*(2), 150–156. https://doi.org/10.1038/ngeo2865

Podladchikov, Y. Y., & Miller, S. A. (2013). Episodic slip and waves of fluid-filled porosity. In Poromechanics V.https://doi.org/10.1061/9780784412992.095

Poli, S., & Schmidt, M. W. (2002). Petrology of subducted slabs. *Annual Review of Earth and Planetary Sciences*, *30*(1), 207–235. https://doi.org/10.1146/annurev.earth.30.091201.140550

Rondenay, S., Abers, G. A., & van Keken, P. E. (2008). Seismic imaging of subduction zone metamorphism. *Geology*, *36*(4), 275. https://doi.org/10.1130/G24112A.1

Saita, H., Nakajima, J., Shiina, T., & Kimura, J.-I. (2015). Slab-derived fluids, fore-arc hydration, and sub-arc magmatism beneath Kyushu, Japan. *Geophysical Research Letters*, *42*, 1685–1693. https://doi.org/10.1002/2015GL063084

Schmalholz, S. M., Medvedev, S., Lechmann, S. M., & Podladchikov, Y. (2014). Relationship between tectonic overpressure, deviatoric stress, driving force, isostasy and gravitational potential energy. *Geophysical Journal International*, *197*(2), 680–696. https://doi.org/10.1093/gji/ggu040

Schurr, B., Asch, G., Rietbrock, A., Trumbull, R., & Haberland, C. (2003). Complex patterns of fluid and melt transport in the central Andean subduction zone revealed by attenuation tomography. *Earth and Planetary Science Letters*, *215*(1-2), 105–119. https://doi.org/10.1016/S0012-821X(03)00441-2

Skarbek, R. M., & Rempel, A. W. (2016). Dehydration-induced porosity waves and episodic tremor and slip. *Geochemistry, Geophysics, Geosystems*, *17*, 442–469. https://doi.org/10.1002/2015GC006155

Soyer, W., & Unsworth, M. (2006). Deep electrical structure of the northern Cascadia (British Columbia, Canada) subduction zone: Implications for the distribution of fluids. *Geology*, *34*(1), 53. https://doi.org/10.1130/G21951.1

van Keken, P. E., Hacker, B. R., Syracuse, E. M., & Abers, G. A. (2011). Subduction factory: 4. Depth-dependent flux of H_2O from subducting slabs worldwide. *Journal of Geophysical Research*. https://doi.org/10.1029/2010jb007922

van Keken, P. E., Kiefer, B., & Peacock, S. M. (2002). High-resolution models of subduction zones: Implications for mineral dehydration reactions and the transport of water into the deep mantle. *Geochemistry, Geophysics, Geosystems*, *3*(10), 1056. https://doi.org/10.1029/2001GC000256

Wada, I., & Behn, M. D. (2015). Focusing of upward fluid migration beneath volcanic arcs: Effect of mineral grain size variation in the mantle wedge. *Geochemistry, Geophysics, Geosystems*, *16*, 3905–3923. https://doi.org/10.1002/2015GC005950

Wark, D. A., & Watson, E. B. (1998). Grain-scale permeabilities of texturally equilibrated, monomineralic rocks. *Earth and Planetary Science Letters*, *164*(3-4), 591–605. https://doi.org/10.1016/S0012-821X(98)00252-0

Wark, D. A., Williams, C. A., Bruce Watson, E., & Price, J. D. (2003). Reassessment of pore shapes in microstructurally equilibrated rocks, with implications for permeability of the upper mantle. *Journal of Geophysical Research*, *108*(B1), 2050. https://doi.org/10.1029/2001JB001575

Warren, C. J., Beaumont, C., & Jamieson, R. A. (2008). Deep subduction and rapid exhumation: Role of crustal strength and strain weakening in continental subduction and ultrahigh-pressure rock exhumation. *Tectonics*, TC6002. https://doi.org/10.1029/2008tc002292

Wilson, C. R., Spiegelman, M., van Keken, P. E., & Hacker, B. R. (2014). Fluid flow in subduction zones: The role of solid rheology and compaction pressure. *Earth and Planetary Science Letters*, *401*, 261–274. https://doi.org/10.1016/j.epsl.2014.05.052

Zheng, L., May, D., Gerya, T., & Bostock, M. (2016). Fluid-assisted deformation of the subduction interface: Coupled and decoupled regimes from 2-D hydromechanical modeling. *Journal of Geophysical Research: Solid Earth*, *121*, 6132–6149. https://doi.org/10.1002/2016JB013102

Zhu, W., David, C., & Wong, T.-F. (1995). Network modeling of permeability evolution during cementation and hot isostatic pressing. *Journal of Geophysical Research*, *100*(B8), 15,451–15,464. https://doi.org/10.1029/95JB00958